BMC Cancer

RESEARCH

Open Access

Dual-layer spectral detector CT quantitative parameters and radiomics for predicting spread through air spaces of lung adenocarcinoma: a dual-center study

Pei Huang[1†], Ze Lin[2†], Yingying Qiu[1†], Dan Chen[1], Yiqing Tan[2], Li Fan[3], Pinggui Lei[4], Yuting Liao[5], Minjing Zuo[6,7*] and Bing Fan[1*]

Abstract

Objectives To evaluate the value of quantitative parameters and radiomic features based on dual-layer spectral detector CT (DLCT) in predicting spread through air spaces (STAS) of lung adenocarcinoma (LUAD).

Methods This study analyzed 266 patients with pathologically confirmed LUAD from two medical centers. Patients from center 1 were divided into training ($n=131$) and internal validation ($n=57$) sets, while center 2 ($n=78$) formed the external validation set. Clinical data, conventional imaging features, and DLCT quantitative parameters were analyzed to develop a clinical-radiological model. Radiomic features were extracted from venous-phase images, including conventional images, virtual monoenergetic images (VMI) at 40 keV, 65 keV, and 100 keV, along with iodine density maps, effective atomic number (Zeff) maps, and electron density (ED) maps. The best-performing radiomics model was combined with clinical-radiological predictors to create a nomogram. Model performance was evaluated through ROC analysis, calibration curves, and decision curve analysis.

Results Multivariate analysis revealed that tumor-lung interface and ED values were independent predictive factors in the clinical-radiological model. The optimal radiomics model was constructed based on VMI 40 keV, demonstrating AUCs of 0.899, 0.835, and 0.828 in the training, internal validation, and external validation sets, respectively. The nomogram, which incorporated the VMI 40 keV radiomics signature along with tumor-lung interface and ED values, outperformed the clinical-radiological model in the training set (AUC = 0.910 vs. 0.870; $P=0.018$) and the internal validation set (AUC = 0.868 vs. 0.798; $P=0.046$). While the improvement in the external validation set was not statistically significant (AUC = 0.848 vs. 0.819; $P=0.184$).

†Pei Huang, Ze Lin and Yingying Qiu contributed equally to this work.

*Correspondence:
Minjing Zuo
minjingzuo@163.com
Bing Fan
26171381@qq.com

Full list of author information is available at the end of the article

© The Author(s) 2025. **Open Access** This article is licensed under a Creative Commons Attribution-NonCommercial-NoDerivatives 4.0 International License, which permits any non-commercial use, sharing, distribution and reproduction in any medium or format, as long as you give appropriate credit to the original author(s) and the source, provide a link to the Creative Commons licence, and indicate if you modified the licensed material. You do not have permission under this licence to share adapted material derived from this article or parts of it. The images or other third party material in this article are included in the article's Creative Commons licence, unless indicated otherwise in a credit line to the material. If material is not included in the article's Creative Commons licence and your intended use is not permitted by statutory regulation or exceeds the permitted use, you will need to obtain permission directly from the copyright holder. To view a copy of this licence, visit http://creativecommons.org/licenses/by-nc-nd/4.0/.

Conclusion The nomogram, which integrates conventional imaging features, DLCT quantitative parameters and VMI 40 keV radiomic features, demonstrates promising performance and represents a potential valuable non-invasive tool for the preoperative assessment of STAS in LUAD.

Keywords Dual-layer spectral detector computed tomography, Spread through air spaces, Lung adenocarcinoma, Radiomics, Nomogram

Introduction

The 2015 World Health Organization classification introduced tumor spread through air spaces (STAS) as a novel lung cancer dissemination pattern, defined as micropapillary clusters, solid nests, or single tumor cells in air spaces beyond the tumor boundary [1]. This indicates that lung cancer can exhibit microscopic spread via air spaces. Current research on STAS predominantly focuses on lung adenocarcinoma (LUAD), the most common histologic subtype of lung cancer [2, 3]. Several studies have suggested that certain STAS cases may be false positives caused by artifacts during surgery or pathological specimen preparation [4, 5]. However, substantial evidence confirms STAS as an independent prognostic factor associated with reduced survival and increased recurrence [6, 7]. For example, a previous study demonstrated that lobectomy yields superior survival outcomes compared with sublobar resection in stage I lung adenocarcinoma with STAS [8]. In contrast, sublobar resection remains appropriate for early-stage patients with non-invasive histologic features, as it preserves pulmonary parenchyma and improves postoperative lung function and quality of life [9]. Furthermore, accurate STAS identification is essential for determining optimal margins in patients undergoing stereotactic radiotherapy, which critically impacts local recurrence [10].

Postoperative histopathological diagnosis is the gold standard for confirming STAS. Currently, there is no reliable method for detecting STAS through preoperative biopsy or intraoperative frozen section [11, 12], which may limit its substantial impact on treatment decisions. Therefore, the development of a non-invasive, simple, and practical method to accurately predict STAS preoperatively could provide crucial information to guide clinical decision-making.

In clinical practice, owing to its superior resolution and cost-effectiveness, high-resolution CT has become the preferred preoperative imaging method for pulmonary lesions. Previous research has demonstrated a correlation between some conventional imaging characteristics of LUAD and the presence of STAS [2, 13], but these features are largely dependent on the subjective experience of the interpreter, which may lead to potential bias. Recent advances in dual-layer spectral detector CT (DLCT) have transformed CT diagnosis from qualitative to quantitative assessment [14, 15]. Beyond conventional images, DLCT produces energy-specific data such as virtual monoenergetic images (VMI), electron density (ED), and iodine density (ID) maps, enhancing diagnostic accuracy and clinical utility [15]. Many studies have shown that quantitative parameters from these images provide more accurate and reliable evidence for the differentiation of pulmonary lesions [16–18]. Additionally, radiomics enables the non-invasive assessment of tumor heterogeneity by rapidly extracting quantitative features from medical images [19]. These features have demonstrated substantial efficacy in differentiating benign from malignant pulmonary lesions, categorizing molecular subtypes, and evaluating prognostic [20, 21]. However, the majority of radiomics research has focused on conventional CT imaging, with the potential usefulness of radiomic features from DLCT images remaining under-explored.

To the best of our knowledge, few studies have investigated whether integrating these methods could provide additional benefits for evaluating pulmonary lesions [22, 23]. Furthermore, a significant research gap remains in the evaluation of STAS, where the synergistic value of this integrated diagnostic approach has yet to be effectively validated. Therefore, this study aims to develop a nomogram that integrates clinical data, conventional imaging characteristics, DLCT quantitative parameters, and radiomic features for preoperative prediction of STAS in LUAD.

Materials and methods

Patients

This retrospective study was conducted with the approval of the institutional ethics review board, which granted a waiver for written informed consent. Between September 2023 and July 2024, patients who underwent thoracic contrast-enhanced DLCT scans at Center 1 were included. After applying the specified inclusion and exclusion criteria, the eligible patients were randomly divided into training and internal validation sets at a 7:3 ratio. Similarly, between January 2024 and April 2024, patients from Center 2 who satisfied the same criteria were enrolled to establish the external validation set. Inclusion criteria: (1) postoperative pathology confirmed LUAD, and the status of STAS was determined; (2) initial diagnosis with no prior history of anti-tumor treatment; (3) DLCT scan performed within two weeks before surgery. Exclusion criteria: (1) postoperative pathological diagnosis of adenocarcinoma in situ (AIS), minimally invasive adenocarcinoma (MIA), or other special types

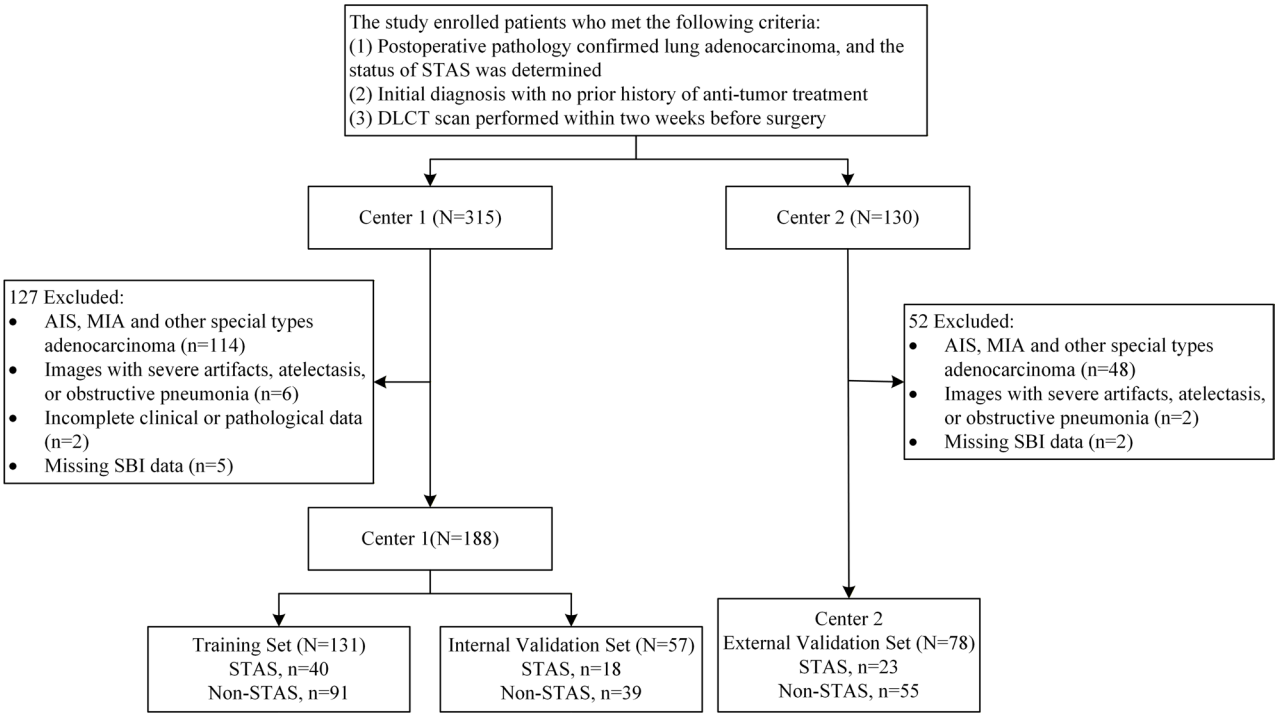


Fig. 1 Flowchart for patient selection. STAS spread through air spaces, DLCT dual-layer spectral detector CT, AIS adenocarcinoma in situ, MIA minimally invasive adenocarcinoma, SBI spectral-based images

such as mucinous, fetal, or intestinal-type adenocarcinoma; (2) images exhibiting severe artifacts, atelectasis, or obstructive pneumonia that obscures tumor margins; (3) incomplete clinical or pathological data; and (4) missing spectral-based images (SBI) data. The inclusion and exclusion flowchart for patient selection is shown in Fig. 1.

DLCT scan protocol

DLCT scans were performed using a 256-slice Hawk Spectral CT at Center 1 and a 64-slice IQon Spectral CT at Center 2 (both Philips Healthcare, Netherlands). Detailed information on the DLCT scanning protocol and contrast agent injection scheme is provided in Supplementary Table 1. Automatic contrast agent tracking was employed with a threshold of 150 HU. The arterial phase scan was initiated with an 8-second delay, followed by the venous phase scan 35 s after the arterial phase. Following the scan, conventional 120 kVp images and SBI were reconstructed with a 1 mm slice thickness and 1 mm increment, including virtual monoenergetic images (VMI) 40 keV, 65 keV, and 100 keV, iodine density (ID) maps, effective atomic number (Zeff) maps, and electron density (ED) maps.

Clinical data collection and image analysis

Clinical information, such as age, gender, and smoking history, was collected for all patients. Tumor conventional imaging features were independently reviewed by two radiologists (3 and 8 years of chest imaging diagnosis experience) while blinded to pathology. Disagreements were resolved through discussion to reach a consensus. Evaluated conventional radiological features included long-axis diameter (LD), consolidation/tumor ratio (CTR), shape, nodule type (pGGN, mGGN, solid nodule), lobulation, spiculation, air bronchogram, tumor-lung interface, vacuole sign, and pleural indentation.

DLCT quantitative parameter measurement

On Philips post-processing workstation (IntelliSpace Portal, Philips Healthcare), DLCT quantitative parameters were independently measured by two radiologists. Final values were calculated as the average of both measurements. The largest axial plane of the lesion was identified on conventional 120 kVp lung window images (window width 1600 HU, window level – 600 HU) in the venous-phase. The region of interest (ROI) for the tumor was then manually outlined along the lesion contour. Large blood vessels, calcification, necrosis, and cavities were carefully avoided when defining the ROI. To maintain consistency across all energy images, the workstation's "copy and paste" function was utilized. Measured quantitative parameters include spectral curve slope (λHU), normalized iodine density (NID), Zeff, and ED value. Additionally, to calculate NID, the ID of the aorta was also recorded at the same axial plane as the tumor.

Supplemental Fig. 1 presents a schematic for DLCT quantitative parameter measurement. λHU and NID were calculated as:

$$\lambda HU = \frac{(CT_{40keV} - CT_{100keV})}{100 - 40}$$

$$NID = \frac{ID_{tumor}}{ID_{aorta}}$$

Clinical-radiological model construction

Following the measurement of the above-mentioned clinical information, conventional imaging characteristics, and DLCT quantitative parameters, univariate and multivariate logistic regression analyses were conducted to construct a clinical-radiological model.

Tumor delineation and radiomics feature extraction

A radiologist manually delineated the three-dimensional ROI of the tumor on the conventional venous-phase images via ITK-SNAP (version 3.8.0). Radiomic features were extracted from seven type images: conventional, VMI at 40 keV, 65 keV, and 100 keV, ID, Zeff, and ED. Since all DLCT energy images had the same dimensions, tumor ROI delineation was performed solely on the conventional image, which could be perfectly aligned with the reconstructed energy images. All images were standardized to a voxel size of $1 \times 1 \times 1$ mm^3, and a bin width of 25 was implemented to ensure uniform intensity scaling. The Pyradiomics package (version 3.6.0) was used to extract radiomic features, including first-order, shape, and texture features. Detailed information of these features is provided in Supplemental Appendix S1. Additionally, another radiologist randomly selected 30 patients to delineate the ROI and assess inter-observer reproducibility by calculating the inter-class correlation coefficient (ICC).

Radiomics feature selection and model construction

Radiomic features with an ICC ≥ 0.75, reflecting good reproducibility, were retained for further analysis. These features were subsequently standardized to Z-scores to ensure comparability across different scales. A three-step approach was employed to refine feature selection within the training dataset. First, features with P-value < 0.05 were selected using the Mann-Whitney U test. Second, to address collinearity among features, Pearson's correlation analysis was performed. When the correlation coefficient between two features exceeded 0.9, one of the correlated features was excluded. Finally, the least absolute shrinkage and selection operator (LASSO) algorithm, with 5-fold cross-validation, was applied to identify the optimal feature set. Based on these selected features from each type image, radiomics models were constructed using a logistic regression (LR) machine learning classifier, resulting in seven distinct radiomic signatures (Rad-sig).

Finally, the Rad-sig from the best-performing radiomics model was combined with independent predictive factors from the clinical-radiological model to develop a nomogram. The entire study workflow is depicted in Fig. 2. This study was conducted in accordance with the Check-List for EvaluAtion of Radiomics research (CLEAR) guidelines [24].

Statistical analysis

Statistical analyses were performed using Python (version 3.7.0), SPSS (version 26.0) and R (version 4.1.0) software. Continuous variables were assessed for normality with the Shapiro-Wilk test and for variance homogeneity with the Levene test. Normally distributed variables were analyzed using parametric tests (t-test or analysis of variance), while nonparametric alternatives (Mann-Whitney U test and Kruskal-Wallis test) were applied to non-normally distributed variables. Categorical data were analyzed using either the Chi-square or Fisher's exact tests. For multiple comparisons, the Bonferroni correction method was used for adjustment. Statistical significance was defined as $P < 0.05$. Receiver operating characteristic (ROC) curve analysis was performed to evaluate model performance in predicting STAS, with calculation of sensitivity, specificity, accuracy, and area under the curve (AUC). The DeLong test was used to compare AUC values between models. Calibration curves and the Hosmer-Lemeshow test assessed agreement between predicted probabilities and observed outcomes. Decision curve analysis (DCA) evaluated the clinical net benefit of the models.

Results

Patient characteristics

A total of 266 patients diagnosed with LUAD (124 Men, 142 Women; ages 35–83 years) were divided into three groups: the training set (131 patients, 40 STAS-positive, 91 STAS-negative), the internal validation set (57 patients, 18 STAS-positive, 39 STAS-negative), and the external validation set (78 patients, 23 STAS-positive, 55 STAS-negative). With the exception of lobulation, which showed a statistically significant difference between the training and external validation sets ($P = 0.032$), no significant differences were observed in the clinical or radiological characteristics across the three cohorts. The baseline characteristics are shown in Table 1.

Clinical-radiological model

Univariate logistic regression analysis of the training dataset revealed several clinical and radiological factors associated with STAS ($P < 0.05$). These factors included

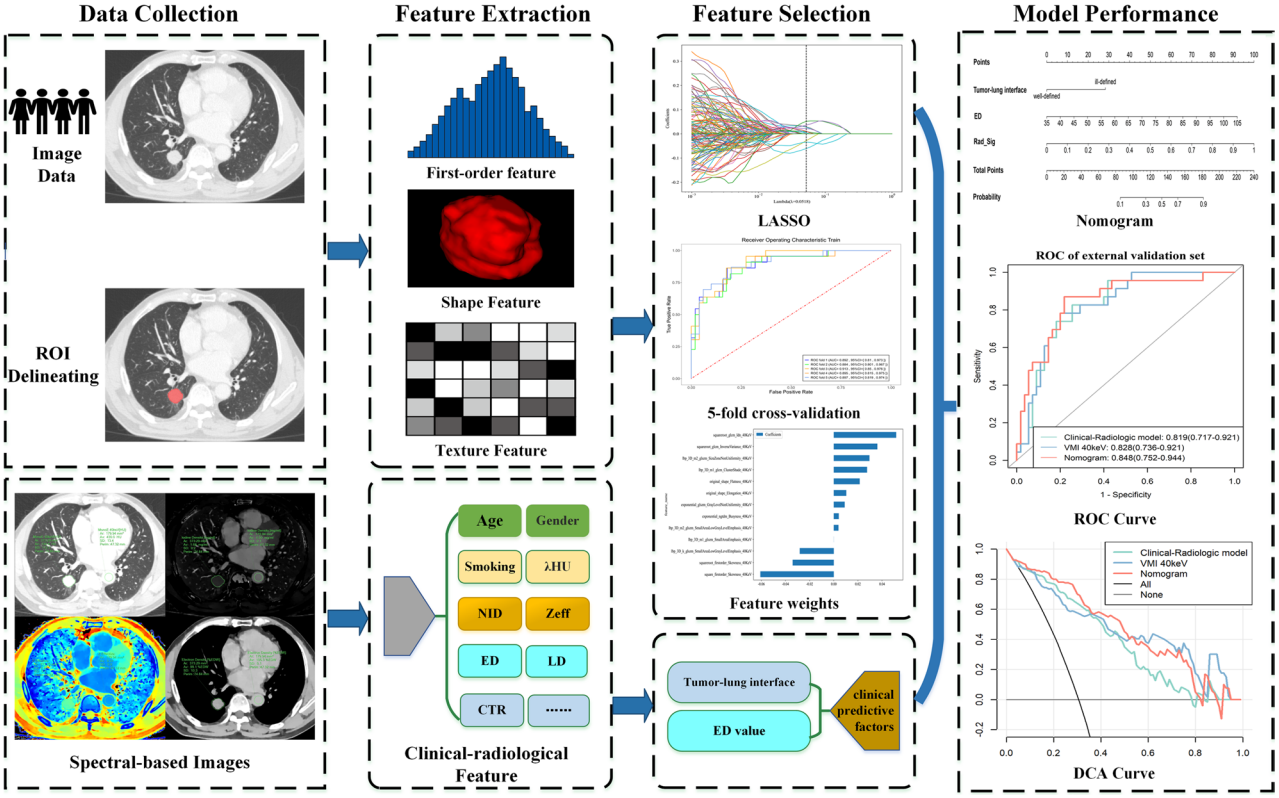


Fig. 2 Overall workflow of this study. ROI region of interest, λHU spectral curve slope, NID normalized iodine density, Zeff effective atomic number, ED electron density, LD long-axis diameter, CTR consolidation/tumor ratio, LASSO least absolute shrinkage and selection operator, ROC receiver operating characteristic, DCA decision curve analysis

tumor LD, CTR, nodule type, tumor-lung interface, pleural indentation, Zeff value, and ED value (Table 2). Following multivariate analysis, tumor-lung interface (OR: 3.54; 95% CI: 1.09–11.46; $P = 0.035$) and ED value (OR: 1.17; 95% CI: 1.02–1.34; $P = 0.028$) were identified as independent predictors of STAS. The clinical-radiological model demonstrated satisfactory predictive performance, with AUCs of 0.870 (95% CI: 0.805–0.935) in the training set, 0.798 (95% CI: 0.675–0.922) in the internal validation set, and 0.819 (95% CI: 0.717–0.921) in the external validation set.

Feature selection and performance of radiomics model

A total of 1,834 radiomic features were extracted from seven imaging modalities: Conventional, VMI 40 keV, 65 keV, 100 keV, ID, Zeff, and ED. LASSO regression identified 14, 13, 14, 19, 19, 8, and 12 features with non-zero coefficients from these modalities, respectively, and the distributions of their coefficients are depicted in Supplemental Fig. 2. An LR classifier was then employed to construct the radiomics model. Figure 3 illustrates ROC curves for the seven models, and Table 3 summarizes their predictive metrics. The models exhibited AUC ranges of 0.847–0.945 (training), 0.751–0.835 (internal validation), and 0.769–0.828 (external validation).

To identify the most suitable model for diagnostic development, we compared the performance of different sequences within the radiomics models. Among these, the VMI 40 keV-based radiomics model demonstrated the best predictive performance, achieving an AUC of 0.899 (95% CI: 0.843–0.955) in the training set, 0.835 (95% CI: 0.711–0.958) in the internal validation set, and 0.828 (95% CI: 0.736–0.921) in the external validation set. Given its consistently superior performance across all datasets, the VMI 40 keV model was selected as the final model for nomogram construction.

Nomogram development and validation

A nomogram (Fig. 4A) was developed by integrating independent predictors (tumor-lung interface and ED value) with the Rad-sig derived from the optimal radiomics model (VMI 40 keV). Compared with the clinical-radiological model, the nomogram achieved higher AUCs for distinguishing STAS (0.910 vs. 0.870, training set; 0.868 vs. 0.798, internal validation set; 0.848 vs. 0.819, external validation set). In the training and internal validation sets, the nomogram showed significantly higher performance than the clinical-radiological model ($P < 0.05$), whereas no significant improvement was observed in the external validation set ($P = 0.184$).

Table 1 Clinical characteristics and radiological parameters

	Training set (*n* = 131)	**Internal Validation Set (*n* = 57)**	**External Validation Set (*n* = 78)**	***P* value**
Age[a]	62(56.0, 69.0)	65(59.0, 71.0)	61(66.0, 69.0)	0.245
Gender				0.198
Man	68(51.91)	22(38.60)	34(43.59)	
Woman	63(48.09)	35(61.40)	44(56.41)	
Smoking history				0.323
No	85(64.89)	37(64.91)	58(74.36)	
YES	46(35.11)	20(35.09)	20(25.64)	
Location				0.671
Left upper lobe	29(22.14)	21(36.84)	25(32.05)	
Left lower lobe	20(15.27)	8(14.04)	12(15.38)	
Right upper lobe	41(31.30)	16(28.07)	21(26.92)	
Right middle lobe	14(10.69)	4(7.02)	6(7.69)	
Right lower lobe	27(20.61)	8(14.04)	14(17.95)	
LD				0.533
≤ 20 mm	59(45.04)	30(52.63)	40(51.28)	
> 20 mm	72(54.96)	27(47.37)	38(48.72)	
CTR[a]	0.64(0.26, 1.00)	0.63(0.34, 1.00)	0.71(0.29, 1.00)	0.812
Nodule type				0.965
pGGN	27(20.61)	10(17.54)	13(16.67)	
mGGN	57(43.51)	26(45.62)	36(46.15)	
Solid nodule	47(35.88)	21(36.84)	29(37.18)	
Lobulation				**0.032**[b]
Absent	45(34.35)	14(24.56)	14(17.95)	
Present	86(65.65)	43(75.44)	64(82.05)	
Spiculation				0.071
Absent	85(64.89)	33(57.89)	38(48.72)	
Present	46(35.11)	24(42.11)	40(51.28)	
Shape				0.333
Round to oval	58(44.27)	31(54.39)	33(42.31)	
Irregular	73(55.73)	26(45.61)	45(57.69)	
Air bronchogram				0.472
Absent	76(58.02)	32(56.14)	51(65.38)	
Present	55(41.98)	25(43.86)	27(34.62)	
Tumor-lung interface				0.785
Well-defined	102(77.86)	45(78.95)	58(74.36)	
Ill-defined	29(22.14)	12(21.05)	20(25.64)	
Vacuole sign				0.948
Absent	103(78.63)	45(78.95)	60(76.92)	
Present	28(21.37)	12(21.05)	18(23.08)	
Pleural indentation				0.220
Absent	68(51.91)	22(38.60)	35(44.87)	
Present	63(48.09)	35(61.40)	43(55.13)	
λHU[a]	2.06(1.71,2.48)	2.00(1.59,2.53)	2.26(1.81,2.77)	0.135
NID	0.36 ± 0.08	0.35 ± 0.10	0.38 ± 0.11	0.089
Zeff	8.52 ± 0.35	8.48 ± 0.37	8.54 ± 0.33	0.616
ED[a]	89.50(67.85, 98.55)	88.00(72.10, 98.30)	92.40(71.40, 97.80)	0.950

LD long-axis diameter, *CTR* consolidation/tumor ratio, *pGGN* pure ground-glass nodule, *mGGN* mixed ground-glass nodule, *λHU* spectral curve slope, *NID* normalized iodine density, *Zeff* effective atomic number, *ED* electron density

[a] Data were presented as medians (25th-75th percentiles) and compared using the Kruskal-Wallis rank sum test

[b] Statistical significance was found between the training and external validation sets

Table 2 Univariate and multivariate logistic regression analyses of clinical-radiological characteristics in training set

Variables	Univariate analysis		Multivariate analysis	
	OR (95%CI)	*P* value	OR (95%CI)	*P* value
Age	1.02 (0.98 ~ 1.06)	0.363		
Gender	1.72 (0.81 ~ 3.66)	0.155		
Smoking history	1.58 (0.73 ~ 3.40)	0.242		
Location				
Left upper lobe	1.00 (Reference)			
Left lower lobe	2.10 (0.61 ~ 7.20)	0.24		
Right upper lobe	1.46 (0.50 ~ 4.28)	0.491		
Right middle lobe	2.36 (0.61 ~ 9.16)	0.216		
Right lower lobe	0.90 (0.26 ~ 3.11)	0.865		
LD	3.50 (1.53 ~ 7.99)	**0.003***	1.54 (0.53 ~ 4.46)	0.431
CTR	142.77(18.92 ~ 1077.15)	**< 0.001***	1.93 (0.02 ~ 242.39)	0.791
Nodule type				
pGGN	1.00 (Reference)		1.00 (Reference)	
mGGN	5.53 (0.67 ~ 45.62)	0.112	0.02 (0.00 ~ 1.46)	0.072
Solid nodule	41.89 (5.23 ~ 335.72)	**< 0.001***	0.01 (0.00 ~ 4.01)	0.139
Lobulation	1.87 (0.82 ~ 4.30)	0.138		
Spiculation	1.16 (0.54 ~ 2.52)	0.705		
Shape	2.03 (0.93 ~ 4.43)	0.074		
Air bronchogram	0.56 (0.26 ~ 1.22)	0.147		
Tumor-lung interface	3.30 (1.40 ~ 7.77)	**0.006***	3.54 (1.09 ~ 11.46)	**0.035***
Vacuole sign	1.65 (0.69 ~ 3.95)	0.259		
Pleural indentation	2.71 (1.25 ~ 5.87)	**0.011***	0.74 (0.25 ~ 2.20)	0.594
λHU	0.66 (0.35 ~ 1.25)	0.203		
NID	6.48 (0.07 ~ 591.82)	0.417		
Zeff	0.05 (0.01 ~ 0.21)	**< 0.001***	0.61 (0.09 ~ 4.24)	0.620
ED	1.13 (1.07 ~ 1.19)	**< 0.001***	1.17 (1.02 ~ 1.34)	**0.028***

LD long-axis diameter, *CTR* consolidation/tumor ratio, *pGGN* pure ground-glass nodule, *mGGN* mixed ground-glass nodule, *λHU* spectral curve slope, *NID* normalized iodine density, *Zeff* effective atomic number, *ED* electron density

* $p < 0.05$

Furthermore, the performance of the nomogram did not differ significantly from that of the radiomics model across all three datasets ($P > 0.05$). Table 4 summarizes the predictive performance of each model, with the associated ROC curves shown in Fig. 4B-D. Results of the DeLong test for each model are provided in Supplemental. The confusion matrices for the nomogram are presented in Supplementary Fig. 4. As shown in Fig. 5A-C, the nomogram demonstrated satisfactory calibration across the three cohorts. The Hosmer–Lemeshow test indicated that the nomogram predictions (training set: $P = 0.383$; internal validation set: $P = 0.125$; external validation set: $P = 0.083$) closely aligned with the actual outcomes, with no significant difference. Decision curve analysis further revealed that, across all datasets, the net benefits of the clinical-radiological, radiomics, and nomogram models generally surpassed those of either treating all patients or not across most reasonable threshold ranges. Additionally, when the risk threshold was less than 0.5, the clinical-radiological model demonstrated a relatively lower overall net benefit (Fig. 5D-F).

Subgroup analysis by nodule type

The nomogram was utilized to predict STAS status in cases presenting as pGGNs/mGGNs and solid nodules. Supplemental Table summarizes the predictive performance of the nomogram across different nodule types. The diagnostic efficacy of the nomogram was slightly higher for pGGNs/mGGNs than for solid nodules. This performance hierarchy was corroborated by AUC values of 0.902 (95% CI: 0.770–1.000) for pGGN/mGGN and 0.749 (95% CI: 0.604–0.894) for solid nodules in the training set; 0.833 (95% CI: 0.619–1.000) and 0.855 (95% CI: 0.680–1.000) in the internal validation set; and 0.847 (95% CI: 0.673–1.000) and 0.781 (95% CI: 0.611–0.951) in the external validation set, respectively.

Discussion

Improving non-invasive and objective methods for distinguishing aggressive subtypes of LUAD, such as STAS, holds significant clinical value. This study evaluated the diagnostic performance of multi-parametric DLCT for identifying STAS. In this dual-center study, we found

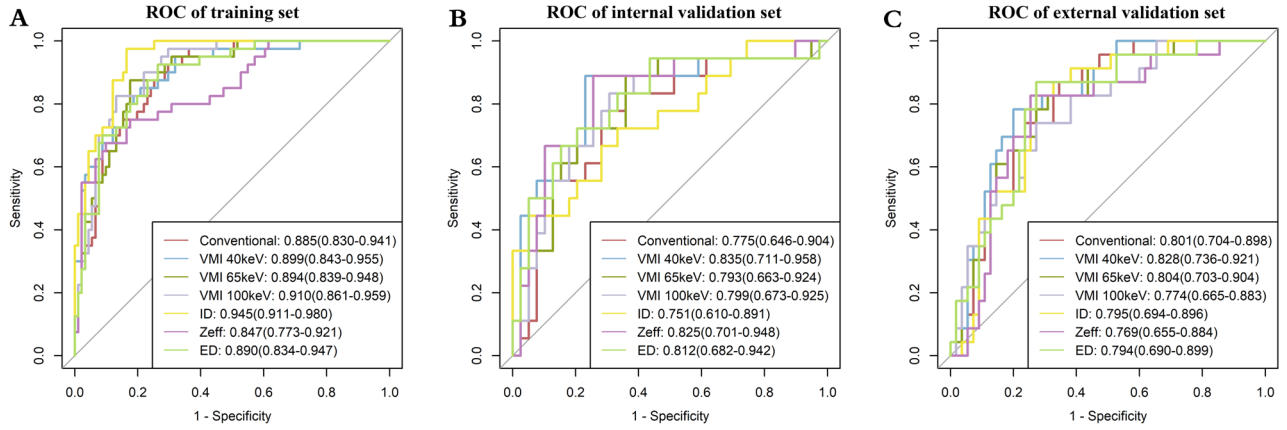


Fig. 3 Receiver operating characteristic curves of different radiomics models in the training set (**A**), internal validation set (**B**), and external validation set (**C**). VMI virtual monoenergetic images, ID iodine density, Zeff effective atomic number, ED electron density

Table 3 Performance of different radiomics models in predicting STAS status of lung adenocarcinoma in the training set, internal validation set, and external validation set

Model	AUC (95% CI)	Accuracy	Sensitivity	Specificity
Training set				
Conventional	0.885 (0.830–0.941)	0.763	0.900	0.703
VMI 40 keV	0.899 (0.843–0.955)	0.802	0.825	0.791
VMI 65 keV	0.894 (0.839–0.948)	0.832	0.850	0.824
VMI 100 keV	0.910 (0.861–0.959)	0.847	0.800	0.868
Iodine density	0.945 (0.911–0.980)	0.870	0.950	0.835
Zeff	0.847 (0.773–0.921)	0.824	0.650	0.901
Electron density	0.890 (0.834–0.947)	0.786	0.900	0.736
Internal validation set				
Conventional	0.775 (0.646–0.904)	0.719	0.722	0.718
VMI 40 keV	0.835 (0.711–0.958)	0.789	0.833	0.769
VMI 65 keV	0.793 (0.663–0.924)	0.702	0.833	0.641
VMI 100 keV	0.799 (0.673–0.925)	0.719	0.778	0.692
Iodine density	0.751 (0.610–0.891)	0.772	0.389	0.949
Zeff	0.825 (0.701–0.948)	0.772	0.833	0.744
Electron density	0.812 (0.682–0.942)	0.754	0.667	0.795
External validation set				
Conventional	0.801 (0.704–0.898)	0.705	0.826	0.655
VMI 40 keV	0.828 (0.736–0.921)	0.782	0.739	0.800
VMI 65 keV	0.804 (0.703–0.904)	0.718	0.783	0.691
VMI 100 keV	0.774 (0.665–0.883)	0.718	0.696	0.727
Iodine density	0.795 (0.694–0.896)	0.756	0.783	0.745
Zeff	0.769 (0.655–0.884)	0.756	0.783	0.745
Electron density	0.794 (0.690–0.899)	0.756	0.826	0.727

STAS spread through air spaces, *AUC* area under the curve, *CI* confidence interval, *VMI* virtual monoenergetic images, *Zeff* effective atomic number

that ED values and tumor-lung interface were independent predictors for identifying STAS. The nomogram that incorporated these two predictive factors, along with the VMI 40 keV radiomics signature, outperformed the clinical-radiological model, providing superior diagnostic accuracy of STAS status in LUAD. Furthermore, it exhibited reasonable predictive performance across different nodule types.

The incidence of STAS in LUAD has been found to vary widely across different studies, with reported rates ranging from 15.7% to 58.4% [13, 25]. In this study, the overall STAS incidence was 30.5%, consistent with previously published studies. Previous studies have shown that certain CT morphological characteristics, such as nodule type, spiculation, air bronchogram, tumor-lung interface and pleural indentation, are related to STAS status [2, 13,

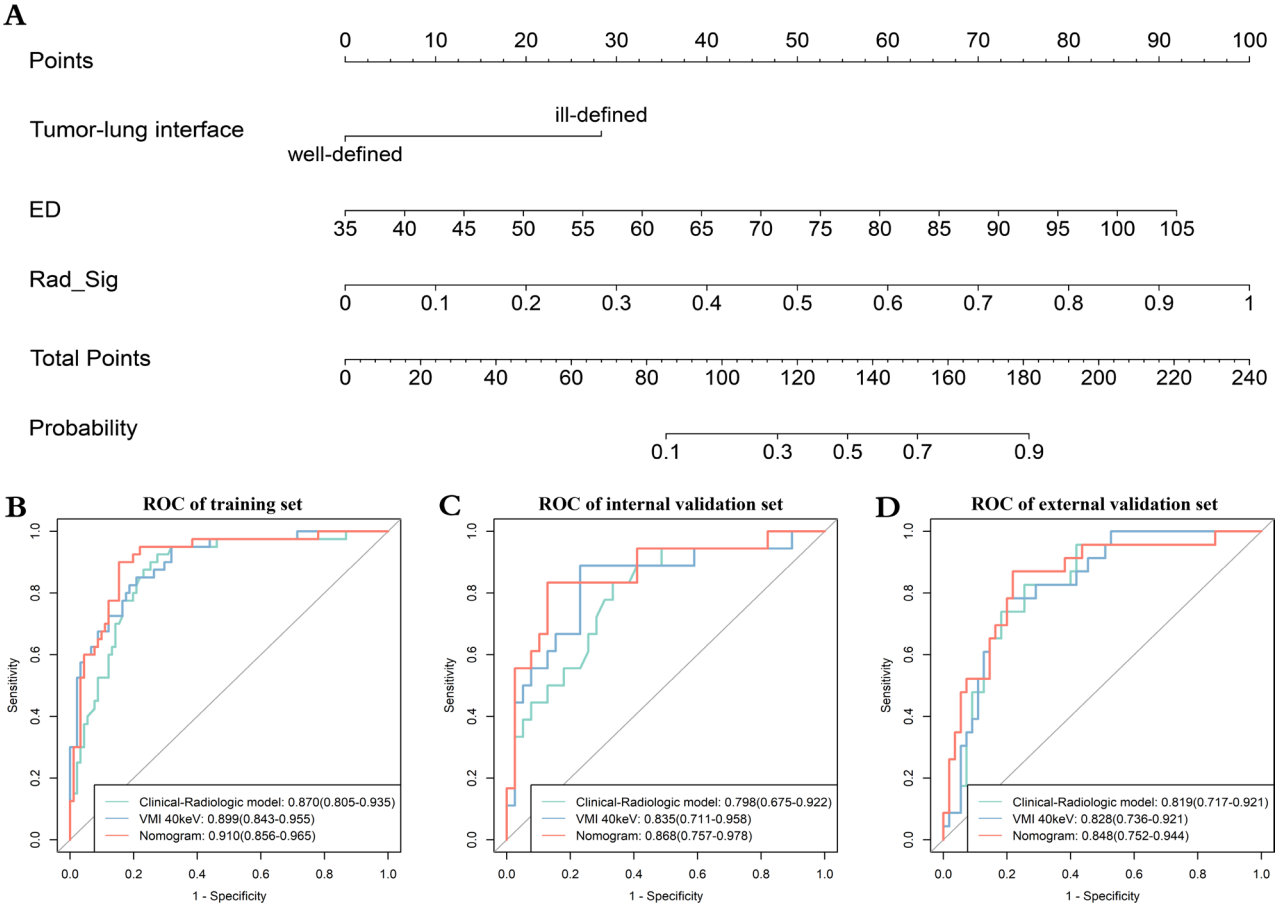


Fig. 4 Nomogram for predicting STAS of lung adenocarcinoma developed based on the training set (**A**). Receiver operating characteristic curves of clinical-radiological model, VMI 40 keV-based radiomics model, and nomogram in the training, internal validation, and external validation sets (**B-D**). STAS spread through air spaces, ED electron density, Rad-Sig radiomics signature, VMI virtual monoenergetic images

26, 27]. The results of this study are generally consistent with these findings, but there are slight differences in spiculation and air bronchogram. The analysis of quantitative parameters, revealed that STAS was significantly related to both increased tumor LD and increased CTR. The work of Kim et al. [2] and Tasnim et al. [28] also supports this result. However, when ED was incorporated into the multivariate analysis, the results indicated that ED was an independent predictor of STAS, whereas CTR was excluded. We speculate that ED, as a DLCT quantitative parameter, may reflect the physical density of the tumor, thereby providing insights into its pathological characteristics [29]. Tumors with a high proportion of solid components typically present higher CT values, which could explain the observed correlation between these characteristics. Therefore, we hypothesize that ED can characterize STAS more effectively than CTR. A study conducted by Liu et al. [17] supported this conclusion, as their model, which utilized LD and venous-phase ED values in 225 patients with LUAD, demonstrated satisfactory performance (AUC = 0.840). However, the absence of an independent validation set limits the assessment of its external applicability. In contrast, the clinical-radiological model in our study, which incorporates tumor-lung interface and ED values, exhibited robust applicability and reliability across diverse datasets.

Most radiomics-related studies have extracted features from conventional CT and PET/CT images to build models [30, 31]. Recently, studies have shifted their focus to the importance of DLCT images in radiomics, suggesting that DLCT image-derived features could enhance model performance [22, 32]. Radiomic features were extracted from a variety of imaging modalities in this study, including conventional images, VMI at 40 keV, 65 keV, and 100 keV, as well as ID, Zeff, and ED maps. Consequently, seven distinct radiomics models were developed. Among these, the model based on VMI 40 keV demonstrated the best performance. Several studies have confirmed that, compared to conventional reconstructed images, VMI 40 keV provides superior tissue contrast, thereby enhancing the accuracy of lesion detection [33, 34]. A previous DLCT imaging study on thoracic tumors demonstrated that VMI in the energy range of 40 to 70 keV have a significantly higher signal-to-noise ratio (SNR) compared to

Table 4 Predictive performance of clinical-radiologic model, radiomics model, and nomogram

Model	AUC (95% CI)	Accuracy	Sensitivity	Specificity
Training set				
Clinical-radiological	0.870 (0.805–0.935)	0.779	0.900	0.725
VMI 40KeV	0.899 (0.843–0.955)	0.802	0.825	0.791
Nomogram	0.910 (0.856–0.965)	0.855	0.875	0.846
Internal validation set				
Clinical-radiological	0.798 (0.675–0.922)	0.702	0.778	0.667
VMI 40KeV	0.835 (0.711–0.958)	0.789	0.833	0.769
Nomogram	0.868 (0.757–0.978)	0.842	0.778	0.872
External validation set				
Clinical-radiological	0.819 (0.717–0.921)	0.756	0.783	0.745
VMI 40KeV	0.828 (0.736–0.921)	0.782	0.739	0.800
Nomogram	0.848 (0.752–0.944)	0.795	0.826	0.782

AUC area under the curve, *CI* confidence interval, *VMI* virtual monoenergetic images

conventional reconstructed images, with the SNR progressively improving as the energy level decreases [35]. In terms of subjective visual assessment, VMI at 40 keV outperformed both 70 keV and conventional reconstructed images [35]. Wang et al. found that among VMI 40–140 keV (with intervals of 10 keV), the deep learning model based on VMI 40 keV outperformed other energy levels in predicting lymph node metastasis in lung cancer [36], which is consistent with our findings. This suggests that imaging at lower energy levels may provide more detailed information about tumor angiogenesis and heterogeneity [36]. These results provide a theoretical foundation for the superiority of the radiomics model based on VMI 40 keV compared to other images.

In our optimal VMI 40 keV radiomics model, the highest-weighted features were the first-order skewness and Gray-Level Co-occurrence Matrix (GLCM) texture features. These features were predominantly derived from square and square-root filtered image transformations. The strong weighting of skewness is highly relevant, as this feature has previously been shown to negatively correlate with tissue density, a finding supported by studies on breast density classification [37]. In our cohort, STAS was significantly associated with an elevated tumor CTR,

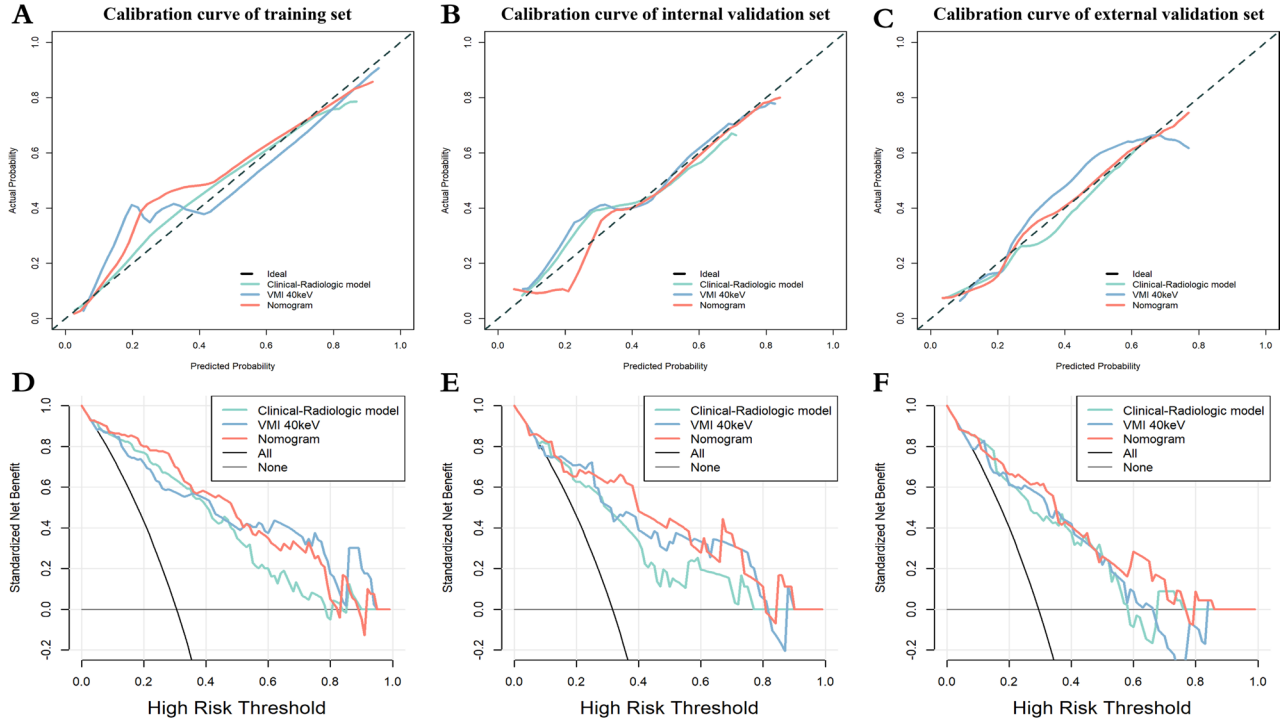


Fig. 5 Calibration curves (**A-C**) and Decision curves analysis (**D-F**) of clinical-radiological model, VMI 40 keV-based radiomics model, and nomogram in the training, internal validation, and external validation sets. VMI virtual monoenergetic images

reflecting increased lesion density. Therefore, based on this mechanistic understanding, lower skewness values may serve as an imaging biomarker for STAS by capturing the underlying increase in density. Moreover, GLCM features detect microstructural patterns by characterizing the spatial relationships of voxel intensities. These texture metrics have been widely validated in assessing tumor heterogeneity and aggressiveness. For instance, Choi et al. [38] demonstrated that GLCM features accurately identify invasive histopathological subtypes of lung adenocarcinoma, and Alibabaei et al. [39] showed that these textural characteristics improve prognostic assessment accuracy for glioblastoma by characterizing tumor heterogeneity.

Additionally, we developed a nomogram that integrates conventional imaging features, DLCT quantitative parameters, and radiomics signature from VMI 40 keV to predict STAS. This nomogram achieved optimal predictive performance, significantly outperforming the clinical-radiological model in both the training and internal validation sets ($P<0.05$). In the external validation cohort, although the nomogram developed demonstrated improvements in performance metrics compared to the clinical-radiological model, these enhancements did not reach statistical significance. This observation may be attributed to potential inter-institutional heterogeneity in the sample population, which could have partially compromised the model's generalizability. Furthermore, when compared to the VMI 40 keV radiomics model, the nomogram did not exhibit a significant advantage. This may be explained by the dominant predictive role of radiomics features in the model, which already achieved a high AUC value. DeLong's test showed no significant difference in diagnostic performance between the nomogram and the radiomics model. Nevertheless, the nomogram demonstrated numerically higher AUC, accuracy, sensitivity, and specificity, suggesting its potential value as a non-invasive decision-support tool in clinical practice. Analysis of misclassifications by the nomogram in the external validation set identified a distinct pattern. False positives were predominantly associated with solid nodules, likely because their high attenuation and homogeneous texture prompt the model to overestimate the likelihood of STAS. Conversely, false negatives occurred more frequently in part-solid nodules, where their complex and heterogeneous internal architecture may obscure the radiomic signature of STAS. These findings underscore that nodule type is a critical contextual factor for interpreting the model's output and represents a key target for future refinement.

This study has certain limitations. First, the relatively small sample size of this retrospective study may introduce potential selection and statistical bias. Second, images were obtained exclusively using the Philips Spectral CT scanner, so the predictive performance and reproducibility of the model with DLCT images acquired from other manufacturers require further validation. Third, the nomogram's performance warrants careful interpretation; its comparable performance to the radiomics model and lack of significant improvement over the clinical-radiological model in the external validation set indicate that its incremental value requires validation in future large-scale, multi-center studies, and such efforts should specifically evaluate its predictive performance within specific subgroups.

In conclusion, we constructed and validated a DLCT-based nomogram, incorporating conventional radiological features, DLCT quantitative parameters, and VMI 40 keV radiomic features. This integrated, non-invasive approach presents a feasible and valuable auxiliary tool that may assist clinicians in the preoperative prediction of STAS for patients with LUAD, thereby supporting personalized clinical decision-making. Nevertheless, the model's external generalizability and its incremental value over radiomics alone require further validation in future studies.

Abbreviations

DLCT	Dual-layer spectral detector CT
STAS	Spread through air spaces
LUAD	Lung adenocarcinoma
VMI	Virtual monoenergetic images
ID	Iodine density
Zeff	Effective atomic number
ED	Electron density
SBI	Spectral-based images
LD	Long-axis diameter
CTR	Consolidation/tumor ratio
ROI	Region of interest
λHU	Spectral curve slope
ICC	Inter-class correlation coefficient
LASSO	Least absolute shrinkage and selection operator
LR	Logistic regression
AUC	Area under the curve
DCA	Decision curve analysis

Supplementary Information

The online version contains supplementary material available at https://doi.org/10.1186/s12885-025-15436-7.

Supplementary Material 1

Acknowledgements

We sincerely thank all the individuals who participated in these studies, as well as the researchers and technicians whose contributions made this work possible.

Authors' contributions

P.H., Z.L., Y.Q. and B.F. conceptualized the study. P.H., Z.L., D.C. and Y.T. organized the database. P.H. and Z.L. wrote the manuscript. P.H., Z.L. and Y.L. performed the statistical analyses. L.F., P.L. and M.Z. provided critical feedback and discussions. B.F. edited the manuscript. M.Z. and B.F. supervised this study. All authors have read and approved the final manuscript.

Funding

This study was supported by the National Natural Science Foundation of China (grant numbers:82160335, 82202140) and the National Key R&D Program of China (grant number: 2022YFC2010002).

Data availability
The datasets used during the current study are available from the corresponding author on reasonable request.

Declarations

Ethics approval and consent to participate
The study was approved by the Ethics Committee of Jiangxi Provincial People's Hospital (ethics approval number: KK-2024-029) and the Second Affiliated Hospital of Nanchang University (ethics approval number: IIT-O-2024-066), following the Declaration of Helsinki. Due to the retrospective nature of the research, the Ethics Committee waived the requirement for informed consent.

Consent for publication
Not applicable.

Competing interests
Yuting Liao is employee of Philips Healthcare (Shanghai, China). The remaining authors of this manuscript declare no relationships with any companies, whose products or services may be related to the subject matter of the article.

Author details
[1]Department of Radiology, Jiangxi Provincial People's Hospital, The First Affiliated Hospital of Nanchang Medical College, Nanchang 330006, China
[2]Department of Radiology, Wuhan Third Hospital, Tongren Hospital of Wuhan University, Wuhan, Hubei, China
[3]Department of Radiology, the Second Affiliated Hospital of Naval Medical University, Shanghai 200003, China
[4]Department of Radiology, the Affiliated Hospital of Guizhou Medical University, Guiyang 550004, China
[5]Clinical & Technical Support, Philips Healthcare, Shanghai, People's Republic of China
[6]Department of Radiology, The Second Affiliated Hospital, Jiangxi Medical College, Nanchang University, Nanchang 330006, China
[7]Jiangxi Provincial Key Laboratory of Intelligent Medical Imaging, Nanchang 330006, China

Received: 17 August 2025 / Accepted: 4 December 2025
Published online: 22 December 2025

References

1. Travis WD, Brambilla E, Nicholson AG, Yatabe Y, Austin JHM, Beasley MB, et al. The 2015 world health organization classification of lung tumors: impact of Genetic, clinical and radiologic advances since the 2004 classification. J THORAC ONCOL. 2015;10(9):1243–60.
2. Kim SK, Kim TJ, Chung MJ, Kim TS, Lee KS, Zo JI, et al. Lung adenocarcinoma: CT features associated with spread through air spaces. Radiology. 2018;289(3):831–40.
3. Toyokawa G, Yamada Y, Tagawa T, Oda Y. Significance of spread through air spaces in early-stage lung adenocarcinomas undergoing limited resection. Thorac Cancer. 2018;9(10):1255–61.
4. Blaauwgeers H, Flieder D, Warth A, Harms A, Monkhorst K, Witte B, et al. A prospective study of loose tissue fragments in Non-Small cell lung cancer resection specimens: an alternative view to spread through air spaces. AM J SURG PATHOL. 2017;41(9):1226–30.
5. Warth A, Muley T, Kossakowski CA, Goeppert B, Schirmacher P, Dienemann H, et al. Prognostic impact of Intra-alveolar tumor spread in pulmonary adenocarcinoma. AM J SURG PATHOL. 2015;39(6):793–801.
6. Aly RG, Rekhtman N, Li X, Takahashi Y, Eguchi T, Tan KS, et al. Spread through air spaces (STAS) is prognostic in atypical Carcinoid, large cell neuroendocrine carcinoma, and small cell carcinoma of the lung. J THORAC ONCOL. 2019;14(9):1583–93.
7. Laville D, Desage AL, Fournel P, Bayle-Bleuez S, Neifer C, Picot T, et al. Spread through air spaces in stage I to III resected lung adenocarcinomas: should the presence of spread through air spaces lead to an upstaging? AM J SURG PATHOL. 2024;48(5):596–604.
8. Eguchi T, Kameda K, Lu S, Bott MJ, Tan KS, Montecalvo J, et al. Lobectomy is associated with better outcomes than sublobar resection in spread through air spaces (STAS)-Positive T1 lung adenocarcinoma: A propensity Score-Matched analysis. J THORAC ONCOL. 2019;14(1):87–98.
9. Altorki N, Wang X, Kozono D, Watt C, Landrenau R, Wigle D, et al. Lobar or sublobar resection for peripheral stage IA Non-Small-Cell lung cancer. NEW ENGL J MED. 2023;388(6):489–98.
10. Loganadane G, Martinetti F, Mercier O, Krhili S, Riet FG, Mbagui R, et al. Stereotactic ablative radiotherapy for early stage non-small cell lung cancer: A critical literature review of predictive factors of relapse. CANCER TREAT REV. 2016;50:240–6.
11. Villalba JA, Shih AR, Sayo T, Kunitoki K, Hung YP, Ly A, et al. Accuracy and reproducibility of intraoperative assessment on tumor spread through air spaces in stage 1 lung adenocarcinomas. J THORAC ONCOL. 2021;16(4):619–29.
12. Zhou F, Villalba JA, Sayo T, Narula N, Pass H, Mino-Kenudson M, et al. Assessment of the feasibility of frozen sections for the detection of spread through air spaces (STAS) in pulmonary adenocarcinoma. Mod PATHOL. 2022;35(2):210–7.
13. Toyokawa G, Yamada Y, Tagawa T, Kamitani T, Yamasaki Y, Shimokawa M, et al. Computed tomography features of resected lung adenocarcinomas with spread through air spaces. J THORAC CARDIOV SUR. 2018;156(4):1670–6.
14. Moore J, Remy J, Altschul E, Chusid J, Flohr T, Raoof S, et al. Thoracic applications of spectral CT scan. Chest. 2024;165(2):417–30.
15. Agostini A, Borgheresi A, Mari A, Floridi C, Bruno F, Carotti M, et al. Dual-energy CT: theoretical principles and clinical applications. RADIOL MED. 2019;124(12):1281–95.
16. Ha T, Kim W, Cha J, Lee YH, Seo HS, Park SY, et al. Differentiating pulmonary metastasis from benign lung nodules in thyroid cancer patients using dual-energy CT parameters. EUR RADIOL. 2022;32(3):1902–11.
17. Liu BC, Ma HY, Huang J, Luo YW, Zhang WB, Deng WW, et al. Does dual-layer spectral detector CT provide added value in predicting spread through air spaces in lung adenocarcinoma? A preliminary study. EUR RADIOL. 2024;34(6):4176–86.
18. Wu F, Zhou H, Li F, Wang JT, Ai T. Spectral CT imaging of lung cancer: quantitative analysis of spectral parameters and their correlation with tumor characteristics. Acad Radiol. 2018;25(11):1398–404.
19. Mayerhoefer ME, Materka A, Langs G, Haggstrom I, Szczypinski P, Gibbs P, et al. Introduction to radiomics. J NUCL MED. 2020;61(4):488–95.
20. Perez-Johnston R, Araujo-Filho JA, Connolly JG, Caso R, Whiting K, Tan KS, et al. CT-based radiogenomic analysis of clinical stage I lung adenocarcinoma with histopathologic features and oncologic outcomes. Radiology. 2022;303(3):664–72.
21. Choi W, Oh JH, Riyahi S, Liu CJ, Jiang F, Chen W, et al. Radiomics analysis of pulmonary nodules in low-dose CT for early detection of lung cancer. MED PHYS. 2018;45(4):1537–49.
22. Xu H, Zhu N, Yue Y, Guo Y, Wen Q, Gao L, et al. Spectral CT-based radiomics signature for distinguishing malignant pulmonary nodules from benign. BMC Cancer. 2023;23(1):91.
23. Lin Z, Liu Y, Xia C, Huang P, Peng Z, Yi L, et al. Dual-energy CT radiomics combined with quantitative parameters for differentiating lung adenocarcinoma from squamous cell carcinoma: A Dual-center study. ACAD RADIOL. 2025;32(3):1675–84.
24. Kocak B, Baessler B, Bakas S, Cuocolo R, Fedorov A, Maier-Hein L, et al. CheckList for evaluation of radiomics research (CLEAR): a step-by-step reporting guideline for authors and reviewers endorsed by ESR and EuSoMII. INSIGHTS IMAGING. 2023;14(1):75.
25. Shiono S, Endo M, Suzuki K, Yanagawa N. Spread through air spaces affects survival and recurrence of patients with clinical stage IA non-small cell lung cancer after wedge resection. J Thorac Dis. 2020;12(5):2247–60.
26. Qi L, Xue K, Cai Y, Lu J, Li X, Li M. Predictors of CT morphologic features to identify spread through air spaces preoperatively in Small-Sized lung adenocarcinoma. FRONT ONCOL. 2020;10:548430.
27. Zhang X, Qiao W, Shen J, Jiang Q, Pan C, Wang Y, et al. Clinical, pathological, and computed tomography morphological features of lung cancer with spread through air spaces. TRANSL LUNG CANCER R. 2024;13(10):2802–12.
28. Tasnim S, Raja S, Mukhopadhyay S, Blackstone EH, Toth AJ, Barron JO, et al. Preoperative predictors of spread through air spaces in lung cancer. J THORAC CARDIOV SUR. 2024;168(3):660–9.
29. Tatsugami F, Higaki T, Kiguchi M, Tsushima S, Taniguchi A, Kaichi Y, et al. Measurement of electron density and effective atomic number by dual-energy scan using a 320-detector computed tomography scanner with Raw data-based analysis: a Phantom study. J COMPUT ASSIST TOMO. 2014;38(6):824–7.
30. Guo R, Yan W, Wang F, Su H, Meng X, Xie Q, et al. The utility of (18)F-FDG PET/CT for predicting the pathological response and prognosis to neoadjuvant

immunochemotherapy in resectable non-small-cell lung cancer. Cancer Imaging. 2024;24(1):120.
31. Dong Y, Jiang Z, Li C, Dong S, Zhang S, Lv Y, et al. Development and validation of novel radiomics-based nomograms for the prediction of EGFR mutations and Ki-67 proliferation index in non-small cell lung cancer. QUANT IMAG MED SURG. 2022;12(5):2658–71.
32. Li M, Fan Y, You H, Li C, Luo M, Zhou J, et al. Dual-Energy CT deep learning radiomics to predict Macrotrabecular-Massive hepatocellular carcinoma. Radiology. 2023;308(2):e230255.
33. Nagayama Y, Tanoue S, Inoue T, Oda S, Nakaura T, Utsunomiya D, et al. Dual-layer spectral CT improves image quality of multiphasic pancreas CT in patients with pancreatic ductal adenocarcinoma. EUR RADIOL. 2020;30(1):394–403.
34. Wang X, Liu D, Jiang S, Zeng X, Li L, Yu T, et al. Subjective and objective assessment of monoenergetic and polyenergetic images acquired by Dual-Energy CT in breast cancer. KOREAN J RADIOL. 2021;22(4):502–12.
35. Doerner J, Hauger M, Hickethier T, Byrtus J, Wybranski C, Grosse HN, et al. Image quality evaluation of dual-layer spectral detector CT of the chest and comparison with conventional CT imaging. EUR J RADIOL. 2017;93:52–8.
36. Wang YW, Chen CJ, Wang TC, Huang HC, Chen HM, Shih JY, et al. Multi-energy level fusion for nodal metastasis classification of primary lung tumor on dual energy CT using deep learning. COMPUT BIOL MED. 2022;141:105185.
37. Landsmann A, Ruppert C, Wieler J, Hejduk P, Ciritsis A, Borkowski K, et al. Radiomics in photon-counting dedicated breast CT: potential of texture analysis for breast density classification. EUR RADIOL EXP. 2022;6(1):30.
38. Choi W, Liu C, Alam SR, Oh JH, Vaghjiani R, Humm J, et al. Preoperative (18) F-FDG PET/CT and CT radiomics for identifying aggressive histopathological subtypes in early stage lung adenocarcinoma. COMPUT STRUCT BIOTEC. 2023;21:5601–8.
39. Alibabaei S, Yousefipour M, Rahmani M, Raminfard S, Tahmasbi M. Evaluating machine learning models for post-surgery treatment response assessment in glioblastoma multiforme: a comparative study of Gray level co-occurrence matrix (GLCM), curvelet, and combined radiomics features selected by multiple algorithms. BMC MED IMAGING. 2025;25(1):362.

Publisher's Note

Springer Nature remains neutral with regard to jurisdictional claims in published maps and institutional affiliations.